

This item is the archived peer-reviewed author-version of:

Achieving high moisture tolerance in pseudohalide perovskite nanocrystals for light-emitting diode application

Reference:

Bhatia Harshita, Keshavarz Masoumeh, Martin Cristina, Van Gaal Liam, Zhang Yiyue, De Coen Brend, Schrenker Nadine, Valli Donato, Ottesen Martin, Bremholm Martin, ...- Achieving high moisture tolerance in pseudohalide perovskite nanocrystals for light-emitting diode application
ACS applied optical materials - ISSN 2771-9855 - 1:6(2023), p. 1184-1191
Full text (Publisher's DOI): <https://doi.org/10.1021/ACSAOM.3C00096>
To cite this reference: <https://hdl.handle.net/10067/2010110151162165141>

Achieving High Moisture-Tolerance in Pseudo-Halide Perovskite Nanocrystals for Light Emitting Diode Application

Harshita Bhatia,^a Masoumeh Keshavarz,^b Cristina Martin,^c Liam Van Gaal,^a Yiyue Zhang,^a Brend de Coen,^d Nadine J. Schrenker,^d Donato Valli,^a Martin Ottesen,^e Martin Bremholm,^e Joris Van de Vondel,^f Sara Bals,^d Johan Hofkens,^a and Elke Debroye^{a*}

^a Department of Chemistry, KU Leuven, Celestijnenlaan 200F, 3001 Leuven, Belgium

^b KU Leuven Institute for Micro- and Nanoscale integration, Celestijnenlaan 200F, 3001 Leuven, Belgium and Micro and Nano Systems, Kasteelpark Arenberg 10, 3001 Leuven

^c Department of Physical Chemistry, Faculty of Pharmacy, University of Castilla-La Mancha, C/ José María Sánchez Ibañez s/n, 02071, Albacete, Spain

^d Electron Microscopy for Materials Science (EMAT) and NANOLab Center of Excellence, University of Antwerp, Groenenborgerlaan 171, B-2020 Wilrijk, Belgium

^e Department of Chemistry and iNANO, Aarhus University, Langelandsgade 140, 8000 Aarhus C, Denmark

^f Quantum Solid-State Physics (QSP), Department of Physics and Astronomy, KU Leuven, Celestijnenlaan 200D, Leuven 3001, Belgium

*corresponding author, email address: elke.debroye@kuleuven.be

Supporting Information Placeholder

ABSTRACT: The addition of potassium thiocyanate (KSCN) to the FAPbBr₃ structure and subsequent post-treatment of the nanocrystals (NCs) lead to high quantum confinement, resulting in a photoluminescent quantum yield (PLQY) approaching unity and microsecond decay times. This synergistic approach demonstrated exceptional stability under humid conditions, retaining 70% of the PLQY for over a month, while the untreated NCs degrade within 24 hours. Additionally, the devices incorporating post-treated NCs displayed 1.5% external quantum efficiency (EQE), a fivefold improvement over untreated devices. These results provide promising opportunities for the use of perovskites in moisture-stable optoelectronics.

KEYWORDS: *lead halide perovskites, surface defects, pseudo-halide, post-treatment, light emitting diodes, spectroscopy*

Perovskite light emitting diodes (PeLEDs) have witnessed a meteoric rise in EQE up to more than 20%, capitalizing on their high PLQY and color purity (full width at half maximum (FWHM) ~ 20 nm).¹ These enticing properties make them strong candidates for future display applications. However, their stability under environmental conditions still lags behind that of commercial LEDs, hindering their commercial deployment.^{2,3} Several strategies have been reported to enhance stability of perovskite NCs, including low-dimensional (2D) structures,^{4,5} doping the ABX₃ with additional cations or anions,^{6,7} or partially substituting halide by thiocyanate, SCN⁻, a pseudo-halide anion. Unlike halides, SCN⁻ forms a stronger ionic and hydrogen bond with Pb²⁺ and the organic A-site cation, respectively, thereby, suppressing halide-related defects.^{8,9} Moreover, significant breakthroughs in the material stability and device performance have been exhibited by regulating surface defects, making surface passivation of perovskites NCs a vital part of the synthesis. Thus far, surface modification by organic-inorganic ion pairs,¹⁰ benzoic acid,¹¹ or branched structure capping ligands,¹² amongst others, have been

applied to increase the stability against external environment.¹³ However, most of the aforementioned approaches involve electrically insulating organic ligands, which hinders the device performance. Inorganic salts, on the other hand, have been shown to enhance the electrical properties¹⁴ and combat non-radiative recombination, thereby, enhancing the PL performance. However, due to the ionic nature of perovskites, which easily degrade in polar solvents, passivation with inorganic salts becomes challenging from a stability point of view. Nevertheless, efficient passivation have been demonstrated with salts such as, NH₄Br,¹⁵ CsBr,¹⁶ NH₄SCN,^{17,18} ZnBr₂,^{14,19,20} PbBr₂,²¹ etc. However, no studies have been reported so far on the incorporation of pseudo-halides in FAPbBr₃ NCs to passivate the defects.

To further surmount the ambient stability concerns and boost the optoelectronic properties of perovskite NCs, herein, we synthesize small-sized KSCN doped FAPbBr₃ NCs following a modified ligand assisted re-precipitation (LARP) approach. Interestingly, the structure was transformed from a dominant 3D to quasi 2D/3D structure upon KSCN addition, which enhanced the stability and optical performance of perovskite NCs. To avoid longer-term degradation, the surface defects were further passivated using a mixture of FABr and ZnBr₂, leading to an increase in PLQY from 30% to 98% and improved shelf-life (over a month under humidity-induced conditions). Overall, the ambient stability was considerably intensified compared with that of untreated NCs. Finally, the post-treated NCs exhibited delayed luminescence (on the scale of 1 μs)²² and a fivefold higher EQE as compared to untreated NCs. These features correlate to improved crystallinity and enhanced long-term stability, which is favorable for all kinds of optoelectronic applications.

Results and Discussion

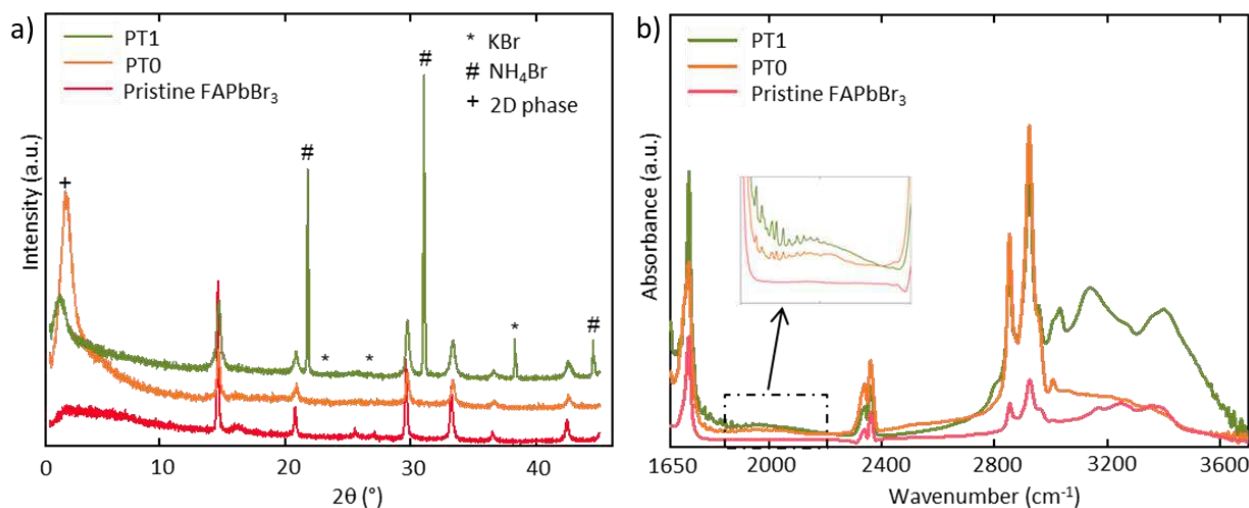


Figure 1. a) XRD pattern and b) FTIR spectra of pristine, PT0, and PT1. The symbol *, #, and + in panel a) represent side phases belonging to KBr, NH_4Br , and 2D perovskites, respectively.

Herein, in the typical synthesis, a stoichiometric ratio of FABr and PbBr_2 , and a 5:1 ratio of PbBr_2 : KSCN are dissolved in DMF. Meanwhile, a mixture of ligands, *sec*-butylamine (*s*-BA) and oleic acid (OAc), is added to the toluene. Finally, the injection of precursor solution into toluene yields a blue-green emissive suspension under UV illumination. Note that the suspension is only slightly emissive immediately after the synthesis. As the precipitate settles down, the supernatant begins to crystallize, turning from blue-green to bright green emission. The blue-green color suggests a low dimensional structure, possibly induced by the incorporation of SCN^- or the protonation of *s*-BA to *sec*-butylammonium.²³ The green emitting supernatant, exclusively containing small NCs, was extracted and post-treated with a mixture of ZnBr_2 and FABr in hexane, containing oleylamine (OAm) and OAc ligands. The untreated and post-treated KSCN: FABr Br_3 NCs will, hereafter, be referred to as PT0 and PT1, respectively.

The crystallographic properties of pristine, PT0, and PT1 NCs are analyzed using X-ray diffraction (XRD). As seen in Figure 1a, NCs exhibit the featured diffraction peaks at 14.7 and 28.6°, typically belonging to the (100) and (200) planes of cubic perovskite crystals, respectively.^{24–26} However, upon KSCN incorporation, three observations were made: (i) Three new peaks appear at 23.1, 25.6, and 38.5°, belonging to the potassium bromide (KBr) phase (marked with *, Figure S1). Notably, its presence was substantially reduced upon extracting the supernatant (Figure 1a and S1).^{27,28,29} (ii) A shift in the XRD pattern towards higher 2θ ($\sim 0.1^\circ$), indicating a contraction of the lattice due to the partial substitution of K^+ by FA^+ . However, it is worth noting that this trend was not observed in the scanning transmission electron microscope (STEM) measurements, which showed lattice expansion upon KSCN doping in FABr Br_3 structure, which is consistent with the literature (Figure S2a and b).^{9,30} This expansion may be attributed to the larger size of the SCN^- ion, which could cause an increase in the lattice parameter.⁹ (iii) An intense peak in the lower 2θ region (2.5°) is also observed, indicating the presence of a low dimensional perovskite structure, which could further contribute to the observed lattice expansion. Subsequently, upon post-treating the NCs, an intense tertiary phase belonging to NH_4Br is also observed (marked with #), owing to the base-catalyzed hydrolysis of FABr.¹⁵ Notably, all these additional phases did not hamper any photophysical properties, but rather enhanced the structural stability, consequently boosting the optoelectronic performance. Moreover, the XRD pattern further shifts to a higher angle, indicating lattice contraction, which is consistent with the STEM results, which also showed a reduction in the lattice pa-

rameter (6.174 Å, Figure S2c) as compared to PT0 (6.201 Å). Additionally, the lattice parameters were calculated along different planes, which revealed that the (100) plane exhibited the largest contraction, followed by the (200) and (110) planes, and so on (Figure S3). The ionic radii of Zn^{2+} and NH_4^+ are smaller as compared to Pb^{2+} or FA^+ , respectively; therefore, Zn^{2+} and NH_4^+ can partially substitute the respective ions or even fill the vacant lattice sites, compensating for the structural defects.

Furthermore, Fourier transform infrared spectroscopy (FTIR) spectroscopy has been employed to confirm the presence of selected functional groups on the surface of pristine, PT0, and PT1 NCs (Figure 1b). The peaks at 1720 cm^{-1} and 3100 - 3400 cm^{-1} can be assigned to C=N and N-H stretching vibrations, respectively, from FA^+ or NH_4^+ cations. While the latter only appears as a low-intensity diffuse absorption band in case of pristine NCs and PT0, PT1 exhibits an intense absorption band, confirming the presence of the ammonium moiety in the post-treated sample. Additionally, due to the low concentration of KSCN in the precursor, only a low-intensity diffuse band around 2030 cm^{-1} can be seen for PT0 (absent for pristine FABr Br_3 NCs), which is attributed to the stretching vibration of the C≡N bond of the SCN^- ion bound to Pb *via* a Pb-S bond.^{33–36} This observation implies the incorporation of SCN^- in FABr Br_3 NCs.^{33–36}

Additionally, the morphology of PT0 and PT1 NCs was studied using high angle annular dark field (HAADF) STEM on day 1 and day 5 of the synthesis (Figure 2a and b). Both samples exhibit mixture of cubic and rectangular NCs. While PT0 revealed highly aggregated NCs with an average size of 10 - 20 nm (Figure S4), PT1 exhibited a well-dispersed morphology with a slight increase in the crystallite size (20 - 40 nm) (Figure S5). Furthermore, the average inter-particle distance for PT0 was around $\sim 0.6 \pm 0.2$ nm, which can be ascribed to the length of the butylamine ligand.³⁷ Notably, the distance increased upon post-treatment (1.6 ± 0.3 nm), owing to the entangled long chain OAc and OAm ligands.^{38,39} While most of the particles were found to be horizontally aligned, a fraction of them were also face-to-face aligned, (Figure S6). In fact, the NCs synthesized with only *s*BA/OAc ligands (PT0) were found to be lying predominately flat on the TEM grids. In general, the interaction between NCs, which is regulated by the length of the hydrocarbon chain, is the key to the self-assembly behavior. It is anticipated that long chain OAm ligand exhibit stronger interaction through interpenetration than short chain *s*-BA ligand, enabling NCs to vertically self-assemble.^{40,41} The standalone, vertical NCs exhibited an average thickness of 3 - 5 nm, equating $n = 4 - 7$ layers in the quasi-2D

structure (Figure S6 and S7). Furthermore, some regions in PT1 consisted of large spherical particles, coated by cubic NCs on the peripheries. The spheres are ascribed to NH_4Br , which tends to crystallize in a cubic structure,⁴² however, forms a more stable spherical shape in apolar hexane due to high surface energy.⁴³ Clearly, both polar NH_4Br and FAPbBr_3 NCs exhibit a tendency to be mutually attracted, thereby forming a heterostructure that resembles a conglomerate. EDX elemental mapping shows that the Pb from FAPbBr_3 NCs is primarily present on the periphery, while N and Br elements constitute the NH_4Br spheres (Figure S8). It should be noted that detecting the presence of sulfur of the SCN^- additive by EDX is challenging since the M Pb peak overlaps with the K-alpha S peak, and the EDX spectra are dominated by the heavy Pb peaks. Accordingly, the electron diffraction pattern for PT1 revealed 3 phases, belonging to cubic FAPbBr_3 , NH_4Br , and KBr , which is consistent with the XRD study (Figure S9). No evidence of ZnBr_2 crystallization in another phase has been observed, however, the elemental mapping indicated the presence of Zn^{2+} in the final product (Figure S8).

Finally, the films were stored under ambient conditions for 5 days and re-imaged to study the aging effect. While the morphology of the PT0 NCs no longer possessed sharp edges and were agglomerated, the PT1 NCs maintained their rectangular and cubic morphology. However, a few NCs exhibited a 'striped pattern', that is, NCs with alternate dark and light contrast (Figure 2d, marked with blue rectangles). The Z-contrast in the HAADF images suggests that the lighter regions correlate to thinner areas of the NCs. It is anticipated that the polar water molecules from air selectively exfoliated the crystal, forming regions with thicker and thinner areas. The thinner regions are anticipated to promote more confinement in the system, which is also noted in the PL study of day 5 (discussed ahead). In such process, the crystal phase transits from high to low symmetry, as also indicated by the splitting of the XRD peaks on day 4 and 5 (Figure S10).

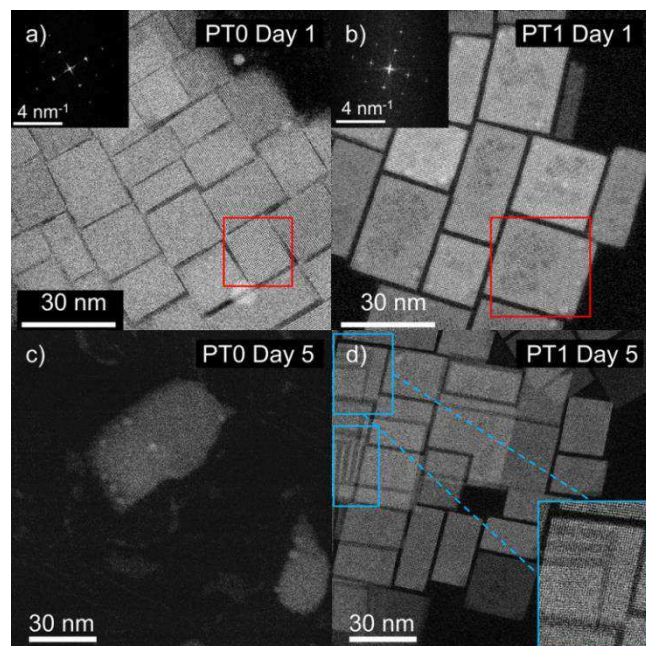


Figure 2. HAADF-STEM images of a) PT0, and b) PT1 on day 1. The insets are the fast-Fourier-transform (FFT) images taken from the regions indicated by the red squares. c) PT0, and d) PT1 on day 5. The blue rectangles indicate the stripping of NCs upon exposure to moisture with an enlarged region of interest.

Next, we evaluate the optical properties of the pristine, PT0, and PT1 NCs on day 1 and day 5. Pristine and PT0 NCs exhibited a wide range of the absorption spectra with emission maxima at 520

nm and 540 nm, respectively (Figure 3a and b). The PL red shift upon KSCN addition is attributed to the partial ion exchange of Br^- with the SCN^- ion, which has stronger binding affinity with Pb^{2+} as compared to Br^- , owing to its larger ionic radius and polarization.³⁵ Interestingly, PT0 NCs exhibit a high PLQY of $\sim 70\%$ at 405 nm excitation, which is two times higher than the pristine NCs, indicating the suppression of non-radiative recombination upon KSCN addition. Additionally, PT0 NCs exhibit three features in the absorption spectrum at 418 nm, 448 nm, and 472 nm along with an absorption band edge at 525 nm, revealing a multi-quantum well structure, having $n = 2, 3, 4,$ and ∞ respectively.⁴⁴ This observation can be correlated with the low angle peak at 2.5° in the XRD pattern, suggesting the existence of a low-dimensional structure (Figure 1a). After storing the films for 5 days under ambient conditions, the PL properties were only slightly altered (e.g., red shift in the emission peak and 10% drop in the PLQY), showing enhanced stability as compared to pristine NCs, which exhibited a red shift of 20 nm in the emission and a PLQY reduction of more than 50%. Notably, previous studies on hybrid perovskites have demonstrated improvement in PLQY upto 60%,^{45,46} whereas inorganic perovskite have shown upto 45%,⁴⁷ suggesting that hybrid perovskite have more potential for further optimization. Upon post-treatment, the absorption spectra exhibited a sharp excitonic peak at 420 nm with an absorption edge at 512 nm, corresponding to the emission peaks at 435 (low intensity) and 520 nm, respectively (Figure 3c). Such sharp excitonic feature is a clear indication of a low-dimensional structure, and is notably more pronounced in PT1 as compared to PT0. The blue shift in the emission maximum as compared to PT0 is attributed to lattice contraction after alloying NH_4^+ and Zn^{2+} at the A and B-sites of the lattice, respectively (verified by a shift towards higher 2θ in XRD, Figure 1a and Figure S2).^{48,49} To probe the different populations of 2D and 3D species, the NCs were selectively excited near the band edge (470 nm) and excitonic peak (405 nm). On one hand, the 2D signature in the absorption and PL spectra hint at a confined structure with high PLQY, 80%, and 98%, when excited at 405 nm and 470 nm, respectively. On the other hand, the 2D structure is generally more prone to defects as compared to 3D. The improved luminescence performance is likely a result of the surface treatment with ZnBr_2 and NH_4Br , passivating surface defects and promoting the radiative recombination of excitons. Upon checking the film on day 5, the emission peak was noted to red-shift by 10 nm, exhibiting a PLQY of 54% and 94% at 405 and 470 nm, respectively. The high stability is attributed to the strong ionic bond between Pb^{2+} and SCN^- ($\text{Pb} \leftarrow \text{SCN}$), which suppresses the defects by reducing the coordination ability of H_2O to Pb compounds, thereby delaying the aging process.⁵⁰ Notably, the PLQY dropped by 26% when excited at 405 nm, while only a drop of 4% is recorded at 470 nm. Particularly, the absorption spectrum for PT1 depicts a simultaneous increase in the sharpness of the 2D excitonic peak as well as 3D band (~ 525 nm) on day 5, where the former could be related to the exfoliation of NCs upon moisture exposure, leaving thicker and thinner regions in the ensemble of NCs (Figure 2d). This observation is also in line with the XRD pattern, recorded over a span of 5 days. The pattern reveals a gradual appearance of broad peaks at low 2θ values ($< 15^\circ$) after 24 hours of exposure to air (Figure S10). Notably, the diffraction peaks exhibit a periodic pattern ($\sim 4.4, 8.8, 11.4^\circ$), corresponding to evenly spaced reflections for $n = 4$. Additionally, the peak at 14.7° also shifts towards low 2θ degrees as the days progress (from day 1 to day 5), suggesting an expansion of lattice. The lattice expansion upon exposure to moisture can be related to an increase in the quantity of lower n-phases, as also previously reported.^{51,52}

The poor resistance of perovskites against moisture or polar solvents has been a major roadblock to widespread applications. To

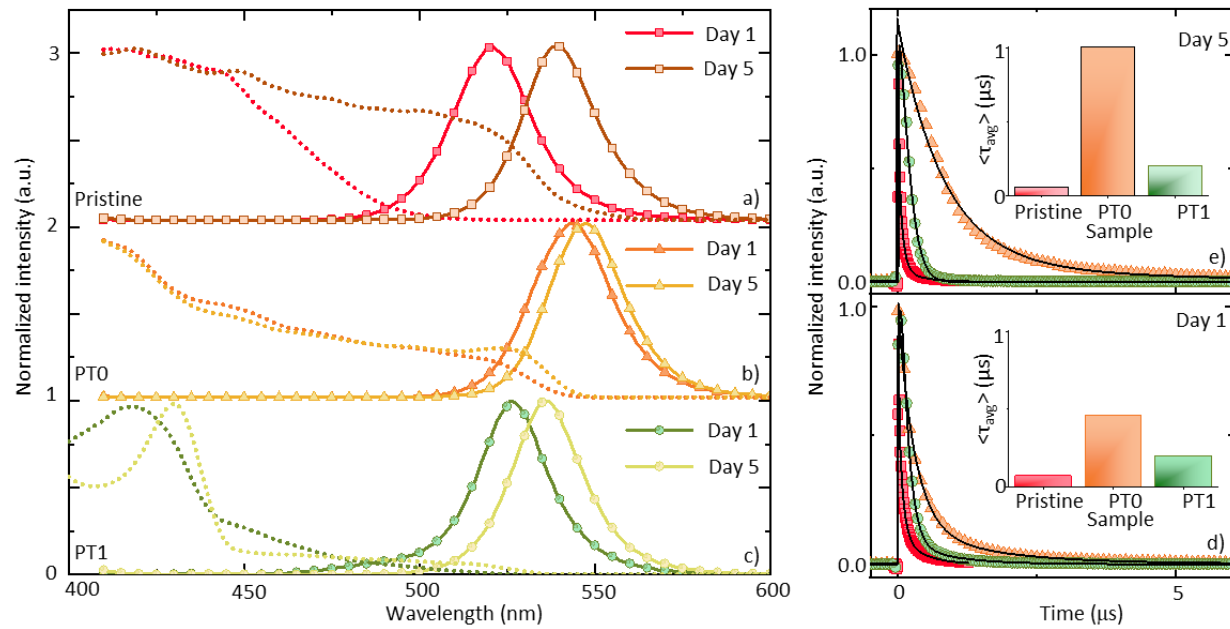


Figure 3. PL (bold lines) and absorption spectra (dashed lines) of a) pristine (day 1), b) PT0, and c) PT1 NCs recorded on day 1 and day 5 (left). TRPL decay of pristine, PT0, and PT1 NCs recorded on d) day 1, and e) day 5 (right). The insets represent the average decay lifetime of pristine, PT0, and PT1 NCs.

evaluate the impact of post-treatment on the stability against moisture, PT0 and PT1 NC films were stored in a controlled humid chamber, containing a saturated solution of MgCl_2 , producing a stable relative humidity level of 37%. The PL measurement was performed on the same film immediately after the synthesis and subsequently repeated after 2h, 3.5h, 5 days, and 30 days. While PT0 NCs exhibit a prompt degradation with a PLQY drop of more than 50% and 85% in 2h and 1 day, respectively, the PT1 NCs remained considerably stable. The PLQY remained unchanged after 2h, followed by a drop of 7% in 3.5h. Strikingly, the PLQY only dropped by ~30% in a span of 30 days, demonstrating an increased stability against moisture (Figure S11). The exceptional stability is attributed to the beneficial effect of post-treatment by NH_4Br and ZnBr_2 , which together passivated the defects at the surface as well as offered a halide-rich environment. The most relevant optoelectronic properties and moisture stability of several perovskite structures have been summarized in Table S1.

Low-temperature PL measurements have been performed to assess the PL pathways in all the samples on day 1 and day 5 (Figure Figure S12). The reduction in thermal energy increases the resolution to distinguish different photoluminescent species in the system. Notably, the data acquired from integrated PL intensity revealed that PT1 is less susceptible to temperature, hinting at passivation of the parasitic non-radiative transitions, resulting in less thermal quenching of the PL intensity compared to pristine and PT0 NCs (Figure S13a and b).

Next, the exciton dynamics was investigated using time-resolved PL (TRPL) decay measurements on pristine, PT0 and PT1 NC films upon 410 nm excitation (Figure 3d, e). The decay spectra are analyzed using a tri-exponential function, and the key findings are summarized in Table S2. Upon comparison of PL decays in PT0 and pristine NCs, NCs on day 1, it can be seen that the average lifetime pristine (τ_{avg}) of PT0 (461 ns) is ~6 times longer than that of pristine NCs, implying the suppression of non-radiative channels upon KSCN incorporation. Notably, the short component τ_1 , which is ascribed to the surface defects-related non-radiative recombination,⁵³ is about two times higher in PT0 than in pristine, owing to the higher surface energy of NCs. However,

the contribution of τ_1 (A_1) substantially declined from 53% to 2%. Upon post-treating the NCs, the τ_{avg} declined by a factor of two as compared to PT0, indicating an increased proportion of a more confined 2D structure (Figure 3c). Nevertheless, the τ_{avg} still remained threefold higher in comparison to pristine NCs. Interestingly, upon aging (day 5), while pristine NC exhibited an obvious reduction in τ_{avg} , PT0 exhibited an unusual twofold enhancement in the lifetime as compared to day 1 (Table S2). This might be ascribed to the agglomeration of NCs (Figure 2c), gradually abolishing the confinement. Another plausible cause for the lengthening of the lifetime can be attributed to a delayed luminescence mechanism, where defects are generated as shallow trap states.^{22,54} Based on time-domain Ab Initio simulations, it was demonstrated that moderate amount of water molecules or humidity usually disrupts the surface of NCs, thereby, localizing the photoexcited electrons just below the conduction band edge or surface. This, in turn, slows down the electron-hole recombination process and also prevents the trapping of electrons in deep trap states.⁵⁵ More importantly, the short component τ_1 (assigned to surface defects) for PT1 did not differ much from day 1, reaffirming the defects stability of post-treated NCs. Notably, the PL decay profile changes from tri-exponential to bi-exponential upon aging, which is an indication of reduction of the exciton recombination processes (assigned as τ_3).¹⁵ This is potentially attributed to the reduction in crystal symmetry (Figure S10), which does not necessarily modify the concentration of surface defects, however, impacts the exciton recombination pathway.

To further confirm the positive effect of the KSCN additive and post-treatment of FAPbBr_3 NCs on the device efficiency, PeLEDs were fabricated using PT0 and PT1 as emissive layers. The devices exhibited electroluminescence at 540 and 523 nm, respectively, with narrow FWHM (~ 1098 cm^{-1} (23 nm)), indicating the structure was retained when external bias was applied. While both the devices exhibited a similar turn-on voltage (~2.4 V), PT1 exhibited a maximum luminance of 275.7 cd m^{-2} at 6.4 V, whereas, PT0 achieved a maximum luminance of 130.1 cd m^{-2} at the same voltage (Figure 4b). The lower luminance intensity is an indication of an emissive layer with a large amount of non-radiative recombination centers, resulting from an excess of defects on the

surface. Interestingly, PT1 also exhibited a fivefold higher EQE (1.5% at

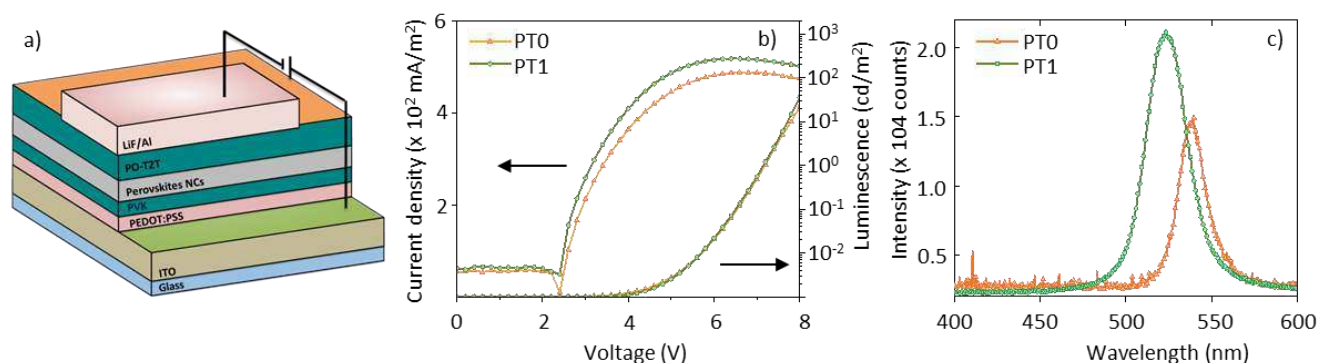


Figure 4. a) Device structure, consisting of glass/ITO/PEDOT/PVK/perovskite/PO-T2T/LiF/Al, where PEDOT, PVK, and PO-T2T refer to poly(3,4-ethylene dioxythiophene), polyvinylcarbazole, and 2,4,6-tris[3-(diphenylphosphino)phenyl]-1,3,5-triazine, respectively, b) I-V response curve, and c) electroluminescence spectra of hybrid multilayer devices, employing PT0 and PT1 NCs as emissive layer at 6.4 V.

523 nm) compared to PT0 (0.3% at 540 nm), which is attributed to the defect healing ability of the salts after post-treatment. Notably, the attained value of EQE for PT1 NCs is six times higher than our previous report on FAPbBr₃ NCs (both proof-of-concept LEDs).¹⁵ These findings demonstrate the positive impact of addition of KSCN to the FAPbBr₃ structure and subsequent post-treatment on the optoelectronic properties of perovskites.

Conclusions

We demonstrated a facile, room-temperature synthesis of quasi-2D KSCN-doped FAPbBr₃ (PT0) NCs, exhibiting improved stability and PLQY by suppressing the non-radiative recombination channels. Upon post-treating the NCs (PT1), the confinement and PLQY were further enhanced, reaching close to unity. Both the NCs exhibited only a slight drop in the PLQY after 5 days, however PT1 also exhibited enhanced 2D features due to humidity-induced exfoliation of NCs, leaving thinner regions in the ensemble. Nevertheless, the post-treatment strategy maintained stability by healing the surface defects formed upon exfoliation. More importantly, PT1 NCs exhibited excellent stability under humidity-induced conditions, remaining highly emissive for more than 30 days, while the PT0 NCs degraded within 24 h of exposure. Finally, PT1 NCs exhibited five times higher EQE as compared to PT0 NCs when employed in PeLEDs, indicating potential for moisture-stable optoelectronics.

Conflicts of interest

There are no conflicts to declare.

Acknowledgements

The authors acknowledge financial support from the Research Foundation - Flanders (FWO Grant Numbers S002019N, 1514220N, G.0B39.15, G.0B49.15, G098319N, and ZW15_09-GOH6316), the KU Leuven Research Fund (C14/19/079, iBOF-21-085 PERSIST and STG/21/010), the Flemish government through long term structural funding Methusalem (CASAS2, Meth/15/04), the Hercules Foundation (HER/11/14) and the ERC through the Marie Curie ITN iSwitch PhD fellowship to H.B. (Grant Number 642196). C.M. acknowledges the financial support: grants PID2021-128761OA-C22 funded by MCIN/AEI/10.13039/501100011033 by the “European Union” and SBPLY/21/180501/000127 funded by JCCM and by the EU through “Fondo Europeo de Desarrollo Regional” (FEDER). D.V.

and N.J.S acknowledge financial support from the Research Foundation - Flanders through doctoral and postdoctoral fellowships, respectively (FWO Grant Numbers 1S45223N and 1238622N). L.V.G. acknowledges the KU Leuven Research Fund for a doctoral fellowship (Grant Number db/21/006/bm, and through iBOF-21-085 PERSIST). S.B. and B.D.C acknowledge financial support from the European Commission by ERC Consolidator grant no. 815128 (REALNANO).

REFERENCES

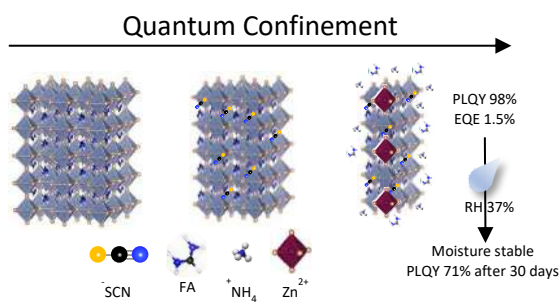
- (1) Bhatia, H.; Ghosh, B.; Debroye, E. Colloidal FAPbBr₃ Perovskite Nanocrystals for Light Emission: What’s Going On? *Journal of Materials Chemistry C* **2022**. <https://doi.org/10.1039/D2TC01373H>.
- (2) Fakharuddin, A.; Gangishetty, M. K.; Abdi-Jalebi, M.; Chin, S.-H.; bin Mohd Yusoff, A. R.; Congreve, D. N.; Tress, W.; Deschler, F.; Vasilopoulou, M.; Bolink, H. J. Perovskite Light-Emitting Diodes. *Nat Electron* **2022**, *5* (4), 203–216. <https://doi.org/10.1038/s41928-022-00745-7>.
- (3) Diao, Z.-L.; Zhang, Y.-W.; Chen, J.-Y.; Tan, W.-Y.; Qian, Y.-N.; Xiao, L.-G.; Min, Y. High-Performance Blue Perovskite Light-Emitting Diodes Enabled by a Sacrificial Agent Maleic Anhydride. *J. Phys. Chem. C* **2022**, *126* (14), 6153–6160. <https://doi.org/10.1021/acs.jpcc.2c00041>.
- (4) Bhatia, H.; Steele, J. A.; Martin, C.; Keshavarz, M.; Solis-Fernandez, G.; Yuan, H.; Fleury, G.; Huang, H.; Dovgaliuk, I.; Chernyshov, D.; Hendrix, J.; Roeyfaers, M. B. J.; Hofkens, J.; Debroye, E. Single-Step Synthesis of Dual Phase Bright Blue-Green Emitting Lead Halide Perovskite Nanocrystal Thin Films. *Chem. Mater.* **2019**, *31* (17), 6824–6832. <https://doi.org/10.1021/acs.chemmater.9b01277>.
- (5) Ali, M. U.; Cai, W.; Cai, J.; Miao, J.; Zhang, S.; Chen, J.; Xiao, L.; Meng, H.; Yan, C.; Wei, G. Enabling Quasi-2D Perovskite-Compatible Growth Environment for Efficient Light-Emitting Diodes. *Advanced Optical Materials* **2022**, *10* (1), 2100671. <https://doi.org/10.1002/adom.202100671>.
- (6) Charles, B.; Dillon, J.; J. Weber, O.; Saiful Islam, M.; T. Weller, M. Understanding the Stability of Mixed A-Cation Lead Iodide Perovskites. *Journal of Materials Chemistry A* **2017**, *5* (43), 22495–22499. <https://doi.org/10.1039/C7TA08617B>.

- (7) Gualdrón-Reyes, Andrés. F.; Yoon, S. J.; Barea, E. M.; Agouram, S.; Muñoz-Sanjosed, V.; Meléndez, Á. M.; Niño-Gómez, M. E.; Mora-Seró, I. Controlling the Phase Segregation in Mixed Halide Perovskites through Nanocrystal Size. *ACS Energy Lett.* **2019**, *4* (1), 54–62. <https://doi.org/10.1021/acsenerylett.8b02207>.
- (8) Zheng, Y.; Yang, S. Stabilization Techniques of Lead Halide Perovskite for Photovoltaic Applications. *Solar RRL* **2022**, *6* (1), 2100710. <https://doi.org/10.1002/solr.202100710>.
- (9) Lou, Y.; Niu, Y.; Yang, D.; Xu, Q.; Hu, Y.; Shen, Y.; Ming, J.; Chen, J.; Zhang, L.; Zhao, Y. Rod-Shaped Thiocyanate-Induced Abnormal Band Gap Broadening in SCN- Doped CsPbBr₃ Perovskite Nanocrystals. *Nano Res.* **2018**, *11* (5), 2715–2723. <https://doi.org/10.1007/s12274-017-1901-z>.
- (10) Kovalenko, M. V.; Bodnarchuk, M. I.; Talapin, D. V. Nanocrystal Superlattices with Thermally Degradable Hybrid Inorganic–Organic Capping Ligands. *J. Am. Chem. Soc.* **2010**, *132* (43), 15124–15126. <https://doi.org/10.1021/ja106841f>.
- (11) Dutt, V. G. V.; Akhil, S.; Singh, R.; Palabathuni, M.; Mishra, N. Year-Long Stability and Near-Unity Photoluminescence Quantum Yield of CsPbBr₃ Perovskite Nanocrystals by Benzoic Acid Post-Treatment. *The Journal of Physical Chemistry C* **2022**. <https://doi.org/10.1021/acs.jpcc.2c01467>.
- (12) Luo, B.; Pu, Y.-C.; Lindley, S. A.; Yang, Y.; Lu, L.; Li, Y.; Li, X.; Zhang, J. Z. Organolead Halide Perovskite Nanocrystals: Branched Capping Ligands Control Crystal Size and Stability. *Angewandte Chemie International Edition* **2016**, *55* (31), 8864–8868. <https://doi.org/10.1002/anie.201602236>.
- (13) Huang, H.; Chen, B.; Wang, Z.; Fu Hung, T.; S. Susha, A.; Zhong, H.; L. Rogach, A. Water Resistant CsPbX₃ Nanocrystals Coated with Polyhedral Oligomeric Silsesquioxane and Their Use as Solid State Luminophores in All-Perovskite White Light-Emitting Devices. *Chemical Science* **2016**, *7* (9), 5699–5703. <https://doi.org/10.1039/C6SC01758D>.
- (14) Song, J.; Fang, T.; Li, J.; Xu, L.; Zhang, F.; Han, B.; Shan, Q.; Zeng, H. Organic–Inorganic Hybrid Passivation Enables Perovskite QLEDs with an EQE of 16.48%. *Advanced Materials* **2018**, *30* (50), 1805409. <https://doi.org/10.1002/adma.201805409>.
- (15) Bhatia, H.; Martin, C.; Keshavarz, M.; Dovgaliuk, I.; Schrenker, N. J.; Ottesen, M.; Qiu, W.; Fron, E.; Bremholm, M.; Van de Vondel, J.; Bals, S.; Roeyfaers, M. B. J.; Hofkens, J.; Debroye, E. Deciphering the Role of Water in Promoting the Optoelectronic Performance of Surface-Engineered Lead Halide Perovskite Nanocrystals. *ACS Appl. Mater. Interfaces* **2023**. <https://doi.org/10.1021/acsmi.2c20605>.
- (16) Lee, J.-W.; Kim, D.-H.; Kim, H.-S.; Seo, S.-W.; Cho, S. M.; Park, N.-G. Formamidinium and Cesium Hybridization for Photo- and Moisture-Stable Perovskite Solar Cell. *Advanced Energy Materials* **2015**, *5* (20), 1501310. <https://doi.org/10.1002/aenm.201501310>.
- (17) Lu, M.; Guo, J.; Lu, P.; Zhang, L.; Zhang, Y.; Dai, Q.; Hu, Y.; Colvin, V. L.; Yu, W. W. Ammonium Thiocyanate-Passivated CsPbI₃ Perovskite Nanocrystals for Efficient Red Light-Emitting Diodes. *J. Phys. Chem. C* **2019**, *123* (37), 22787–22792. <https://doi.org/10.1021/acs.jpcc.9b06144>.
- (18) Yukta; Chavan, R. D.; Yadav, P.; Satapathi, S. Ammonium Thiocyanate-Passivated Quasi-Two-Dimensional Dion Jacobson Perovskite Solar Cells for Improved Efficiency and Stability. *ACS Appl. Energy Mater.* **2022**, *5* (11), 13723–13734. <https://doi.org/10.1021/acsaem.2c02398>.
- (19) De Trizio, L.; Prato, M.; Genovese, A.; Casu, A.; Povia, M.; Simonutti, R.; Alcocer, M. J. P.; D’Andrea, C.; Tassone, F.; Manna, L. Strongly Fluorescent Quaternary Cu–In–Zn–S Nanocrystals Prepared from Cu₁XInS₂ Nanocrystals by Partial Cation Exchange. *Chem. Mater.* **2012**, *24* (12), 2400–2406. <https://doi.org/10.1021/cm301211e>.
- (20) Macdonald, T. J.; Mange, Y. J.; Dewi, M.; McFadden, A.; Skinner, W. M.; Nann, T. Cation Exchange of Aqueous CuInS₂ Quantum Dots. *CrystEngComm* **2014**, *16* (40), 9455–9460. <https://doi.org/10.1039/C4CE00545G>.
- (21) Wang, S.; Wang, W.; Donmez, S.; Xin, Y.; Mattoussi, H. Engineering Highly Fluorescent and Colloidally Stable Blue-Emitting CsPbBr₃ Nanoplatelets Using Polysalt/PbBr₂ Ligands. *Chem. Mater.* **2022**, *34* (11), 4924–4936. <https://doi.org/10.1021/acs.chemmater.2c00082>.
- (22) Chirvony, V. S.; González-Carrero, S.; Suárez, I.; Galian, R. E.; Sessolo, M.; Bolink, H. J.; Martínez-Pastor, J. P.; Pérez-Prieto, J. Delayed Luminescence in Lead Halide Perovskite Nanocrystals. *J. Phys. Chem. C* **2017**, *121* (24), 13381–13390. <https://doi.org/10.1021/acs.jpcc.7b03771>.
- (23) Daub, M.; Hillebrecht, H. Synthesis, Single-Crystal Structure and Characterization of (CH₃NH₃)₂Pb(SCN)₂I₂. *Angewandte Chemie* **2015**, *127* (38), 11168–11169. <https://doi.org/10.1002/ange.201506449>.
- (24) Sutanto, A. A.; Quelo, V. I. E.; Garcia-Benito, I.; Laasonen, K.; Smit, B.; Nazeeruddin, M. K.; Syzgantseva, O. A.; Grancini, G. Pushing the Limit of Cs Incorporation into FAPbBr₃ Perovskite to Enhance Solar Cells Performances. *APL Materials* **2019**, *7* (4), 041110. <https://doi.org/10.1063/1.5087246>.
- (25) Jarmouni, N.; Tomaiuolo, M.; Gabbani, A.; Pineider, F.; Bassam, R.; Belaouad, S.; Benmokhtar, S. Synthesis of Brightly Luminescent Colloidal Formamidinium Lead Bromide Perovskite FAPbBr₃ Nanoplatelets with Tunable Emission. *MATEC Web Conf.* **2021**, *348*, 01015. <https://doi.org/10.1051/mateconf/202134801015>.
- (26) Han, D.; Imran, M.; Zhang, M.; Chang, S.; Wu, X.; Zhang, X.; Tang, J.; Wang, M.; Ali, S.; Li, X.; Yu, G.; Han, J.; Wang, L.; Zou, B.; Zhong, H. Efficient Light-Emitting Diodes Based on in Situ Fabricated FAPbBr₃ Nanocrystals: The Enhancing Role of the Ligand-Assisted Reprecipitation Process. *ACS Nano* **2018**, *12* (8), 8808–8816. <https://doi.org/10.1021/acsnano.8b05172>.
- (27) Kanwat, A.; Yantara, N.; Ng, Y. F.; Hooper, T. J. N.; Rana, P. J. S.; Febriansyah, B.; Harikesh, P. C.; Salim, T.; Vashishtha, P.; Mhaisalkar, S. G.; Mathews, N. Stabilizing the Electroluminescence of Halide Perovskites with Potassium Passivation. *ACS Energy Lett.* **2020**, *5* (6), 1804–1813. <https://doi.org/10.1021/acsenerylett.0c00553>.
- (28) Lin, H.; Wei, Q.; Ng, K. W.; Dong, J.-Y.; Li, J.-L.; Liu, W.-W.; Yan, S.-S.; Chen, S.; Xing, G.-C.; Tang, X.-S.; Tang, Z.-K.; Wang, S.-P. Stable and Efficient Blue-Emitting CsPbBr₃ Nanoplatelets with Potassium Bromide Surface Passivation. *Small* **2021**, *17* (43), 2101359. <https://doi.org/10.1002/sml.202101359>.
- (29) Yang, J.-N.; Song, Y.; Yao, J.-S.; Wang, K.-H.; Wang, J.-J.; Zhu, B.-S.; Yao, M.-M.; Rahman, S. U.; Lan, Y.-F.; Fan, F.-J.; Yao, H.-B. Potassium Bromide Surface Passivation on CsPbI₃-XBr_x Nanocrystals for Efficient and Stable Pure Red Perovskite Light-Emitting Diodes. *J. Am. Chem. Soc.* **2020**, *142* (6), 2956–2967. <https://doi.org/10.1021/jacs.9b11719>.

- (30) Thapa, S.; Adhikari, G. C.; Zhu, H.; Zhu, P. Scalable Synthesis of Highly Luminescent and Stable Thiocyanate Based CsPbX₃ Perovskite Nanocrystals for Efficient White Light-Emitting Diodes. *Journal of Alloys and Compounds* **2021**, *860*, 158501. <https://doi.org/10.1016/j.jallcom.2020.158501>.
- (31) Min, X.; Xie, Q.; Wang, X.; Chen, M. Enhancing the Stability of Cesium Lead Iodide Perovskite Nanocrystals: Recent Progress, Challenges and Opportunities. *Surfaces and Interfaces* **2021**, *22*, 100870. <https://doi.org/10.1016/j.surfin.2020.100870>.
- (32) Yangui, A.; Pillet, S.; Lusson, A.; Bendeif, E.-E.; Triki, S.; Abid, Y.; Boukheddaden, K. Control of the White-Light Emission in the Mixed Two-Dimensional Hybrid Perovskites (C₆H₁₁NH₃)₂[PbBr_{4-x}I_x]. *Journal of Alloys and Compounds* **2017**, *699*, 1122–1133. <https://doi.org/10.1016/j.jallcom.2017.01.032>.
- (33) Wechwithayakhlung, C.; Packwood, D. M.; Chaopaknam, J.; Worakajit, P.; Ittisarnonchai, S.; Chanlek, N.; Promarak, V.; Kongpatpanich, K.; Harding, D. J.; Pattanasattayavong, P. Tin(II) Thiocyanate Sn(NCS)₂ – a Wide Band Gap Coordination Polymer Semiconductor with a 2D Structure. *J. Mater. Chem. C* **2019**, *7* (12), 3452–3462. <https://doi.org/10.1039/C8TC06150E>.
- (34) Yu, D.; Wei, Q.; Li, H.; Xie, J.; Jiang, X.; Pan, T.; Wang, H.; Pan, M.; Zhou, W.; Liu, W.; Chow, P. C. Y.; Ning, Z. Quasi-2D Bilayer Surface Passivation for High Efficiency Narrow Bandgap Perovskite Solar Cells. *Angewandte Chemie International Edition* **2022**, *61* (20), e202202346. <https://doi.org/10.1002/anie.202202346>.
- (35) Kim, H.-Y.; Cho, S.-B.; Hou, B.; Park, I.-K. Silver Thiocyanate Treatment-Induced Enhancement of Photoluminescence Efficiency of CsPbBr₃ Perovskite Quantum Dots. *J. Korean Phys. Soc.* **2022**, *81* (2), 150–157. <https://doi.org/10.1007/s40042-022-00501-2>.
- (36) Cai, T.; Li, F.; Jiang, Y.; Liu, X.; Xia, X.; Wang, X.; Peng, J.; Wang, L.; A. Daoud, W. In Situ Inclusion of Thiocyanate for Highly Luminescent and Stable CH₃NH₃PbBr₃ Perovskite Nanocrystals. *Nanoscale* **2019**, *11* (3), 1319–1325. <https://doi.org/10.1039/C8NR07987K>.
- (37) Beygi, H.; Sajjadi, S. A.; Babakhani, A.; Young, J. F.; van Veggel, F. C. J. M. Solution Phase Surface Functionalization of PbS Nanoparticles with Organic Ligands for Single-Step Deposition of p-Type Layer of Quantum Dot Solar Cells. *Applied Surface Science* **2018**, *459*, 562–571. <https://doi.org/10.1016/j.apsusc.2018.08.056>.
- (38) Soetan, N.; Erwin, W. R.; Tonigan, A. M.; Walker, D. G.; Bardhan, R. Solvent-Assisted Self-Assembly of CsPbBr₃ Perovskite Nanocrystals into One-Dimensional Superlattice. *J. Phys. Chem. C* **2017**, *121* (33), 18186–18194. <https://doi.org/10.1021/acs.jpcc.7b03939>.
- (39) Graf, R. T.; Schlosser, A.; Zámbo, D.; Schlenkrich, J.; Rusch, P.; Chatterjee, A.; Pfnür, H.; Bigall, N. C. Interparticle Distance Variation in Semiconductor Nanoplatelet Stacks. *Advanced Functional Materials* *n/a* (n/a), 2112621. <https://doi.org/10.1002/adfm.202112621>.
- (40) Yuan, Y.; Liu, Z.; Liu, Z.; Peng, L.; Li, Y.; Tang, A. Photoluminescence and Self-Assembly of Cesium Lead Halide Perovskite Nanocrystals: Effects of Chain Length of Organic Amines and Reaction Temperature. *Applied Surface Science* **2017**, *405*, 280–288. <https://doi.org/10.1016/j.apsusc.2017.02.024>.
- (41) Yang, Z.; Peng, S.; Lin, F.; Wang, P.; Xing, G.; Yu, L. Self-Assembly Behavior of Metal Halide Perovskite Nanocrystals. *Chinese Journal of Chemistry* **2022**, *40* (18), 2239–2248. <https://doi.org/10.1002/cjoc.202200161>.
- (42) Goyal, P. S.; Penfold, J.; Tomkinson, J. Observation by Neutron Incoherent Inelastic Spectroscopy of Split Higher Harmonics of the Ammonium Ion Librational Mode in the Cubic Phase of NH₄Br. *Chemical Physics Letters* **1986**, *127* (5), 483–486. [https://doi.org/10.1016/0009-2614\(86\)80594-2](https://doi.org/10.1016/0009-2614(86)80594-2).
- (43) Looby, D.; Griffiths, J. B. Fixed Bed Porous Glass Sphere (Porosphere) Bioreactors for Animal Cells. *Cytotechnology* **1988**, *1* (4), 339–346. <https://doi.org/10.1007/BF00365079>.
- (44) Bekenstein, Y.; Koscher, B. A.; Eaton, S. W.; Yang, P.; Alivisatos, A. P. Highly Luminescent Colloidal Nanoplates of Perovskite Cesium Lead Halide and Their Oriented Assemblies. *J. Am. Chem. Soc.* **2015**, *137* (51), 16008–16011. <https://doi.org/10.1021/jacs.5b11199>.
- (45) Luo, Z.; Liu, B.; Zheng, T.; Luo, X.; Lu, L.; Tian, B.; Xu, P.; Kwok, H. S.; Li, G. High-Efficiency Sky-Blue Perovskite Light-Emitting Diodes via the Trade-Off between the Electron–Phonon Coupling Loss and Defect Passivation. *ACS Photonics* **2022**, *9* (7), 2422–2430. <https://doi.org/10.1021/acsp Photonics.2c00496>.
- (46) Yarita, N.; Tahara, H.; Saruyama, M.; Kawawaki, T.; Sato, R.; Teranishi, T.; Kanemitsu, Y. Impact of Postsynthetic Surface Modification on Photoluminescence Intermittency in Formamidinium Lead Bromide Perovskite Nanocrystals. *J. Phys. Chem. Lett.* **2017**, *8* (24), 6041–6047. <https://doi.org/10.1021/acs.jpcclett.7b02840>.
- (47) Yang, J.-N.; Ma, Z.-Y.; Luo, J.-D.; Wang, J.-J.; Ye, C.; Zhou, Y.; Yin, Y.-C.; Ru, X.-C.; Chen, T.; Li, L.-Y.; Feng, L.-Z.; Song, K.-H.; Ge, J.; Zhang, Q.; Yao, H.-B. Pseudohalogen Resurfaced CsPbBr₃ Nanocrystals for Bright, Efficient, and Stable Green-Light-Emitting Diodes. *Nano Lett.* **2023**. <https://doi.org/10.1021/acs.nanolett.3c00385>.
- (48) Li, R.; Chen, S.; Li, X.; Yin, G.; Gong, Y.; Yu, J.; Pang, G.; Liu, J.; Liu, Y.; Ni, Z.; Zhang, L.; Chen, R.; Wang, H.-L. Zn Doped MAPbBr₃ Single Crystal with Advanced Structural and Optical Stability Achieved by Strain Compensation. *Nanoscale* **2020**, *12* (6), 3692–3700. <https://doi.org/10.1039/C9NR09657D>.
- (49) Deng, J.; Xun, J.; Qin, Y.; Li, M.; He, R. Blue-Emitting NH₄⁺-Doped MAPbBr₃ Perovskite Quantum Dots with near Unity Quantum Yield and Super Stability. *Chem. Commun.* **2020**, *56* (79), 11863–11866. <https://doi.org/10.1039/D0CC04912C>.
- (50) Zhao, J.; He, G.; Yang, D.; Guo, D.; Yang, L.; Chen, J.; Ma, D. Highly Stable and Efficient α -Phase FA-Based Perovskite Solar Cells Prepared in Ambient Air by Strategically Enhancing the Interaction between Ions in Crystal Lattices. *Sustainable Energy & Fuels* **2021**, *5* (17), 4268–4276. <https://doi.org/10.1039/D1SE00784J>.
- (51) Wygant, B. R.; Geberth, G. T.; Ye, A. Z.; Dolocan, A.; Cotton, D. E.; Roberts, S. T.; Vanden Bout, D. A.; Mullins, C. B. Moisture-Driven Formation and Growth of Quasi-2-D Organolead Halide Perovskite Crystallites. *ACS Appl. Energy Mater.* **2020**, *3* (7), 6280–6290. <https://doi.org/10.1021/acsaem.0c00423>.
- (52) Stoumpos, C. C.; Cao, D. H.; Clark, D. J.; Young, J.; Rondinelli, J. M.; Jang, J. I.; Hupp, J. T.; Kanatzidis, M. G. Ruddlesden–Popper Hybrid Lead Iodide Perovskite 2D Homologous Semiconductors. *Chem. Mater.* **2016**, *28* (8), 2852–2867. <https://doi.org/10.1021/acs.chemmater.6b00847>.

- (53) Li, X.; Lian, X.; Pang, J.; Luo, B.; Xiao, Y.; Li, M.-D.; Huang, X.-C.; Zhang, J. Z. Defect-Related Broadband Emission in Two-Dimensional Lead Bromide Perovskite Microsheets. *J. Phys. Chem. Lett.* **2020**, *11* (19), 8157–8163. <https://doi.org/10.1021/acs.jpcclett.0c02355>.
- (54) Chirvony, V. S.; Martínez-Pastor, J. P. Trap-Limited Dynamics of Excited Carriers and Interpretation of the Photoluminescence Decay Kinetics in Metal Halide Perovskites. *J. Phys. Chem. Lett.* **2018**, *9* (17), 4955–4962. <https://doi.org/10.1021/acs.jpcclett.8b01241>.
- (55) Long, R.; Fang, W.; Prezhdo, Oleg. V. Moderate Humidity Delays Electron–Hole Recombination in Hybrid Organic–Inorganic Perovskites: Time-Domain Ab Initio Simulations Rationalize Experiments. *J. Phys. Chem. Lett.* **2016**, *7* (16), 3215–3222. <https://doi.org/10.1021/acs.jpcclett.6b01412>.

TOC



Supporting Information

Achieving High Moisture-Tolerance in Pseudo-Halide Perovskite Nanocrystals for Light Emitting Diode Application

Harshita Bhatia,^a Masoumeh Keshavarz,^b Cristina Martin,^c Liam Van Gaal,^a Yiyue Zhang,^a Brend de Coen,^d Nadine J. Schrenker,^d Donato Valli,^a Martin Ottesen,^e Martin Bremholm,^e Joris Van de Vondel,^f Sara Bals,^d Johan Hofkens,^a and Elke Debroye^{a*}

^a Department of Chemistry, KU Leuven, Celestijnenlaan 200F, 3001 Leuven, Belgium

^b KU Leuven Institute for Micro- and Nanoscale integration, Celestijnenlaan 200F, 3001 Leuven, Belgium and Micro and Nano Systems, Kasteelpark Arenberg 10, 3001 Leuven

^c Department of Physical Chemistry, Faculty of Pharmacy, University of Castilla-La Mancha, C/ José María Sánchez Ibañez s/n, 02071, Albacete, Spain

^d Electron Microscopy for Materials Science (EMAT) and NANOLab Center of Excellence, University of Antwerp, Groenenborgerlaan 171, B-2020 Wilrijk, Belgium

^e Department of Chemistry and iNANO, Aarhus University, Langelandsgade 140, 8000 Aarhus C, Denmark

^f Quantum Solid-State Physics (QSP), Department of Physics and Astronomy, KU Leuven, Celestijnenlaan 200D, Leuven 3001, Belgium

*corresponding author, email address: elke.debroye@kuleuven.be

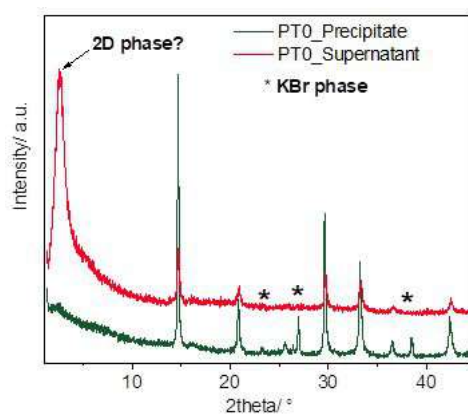
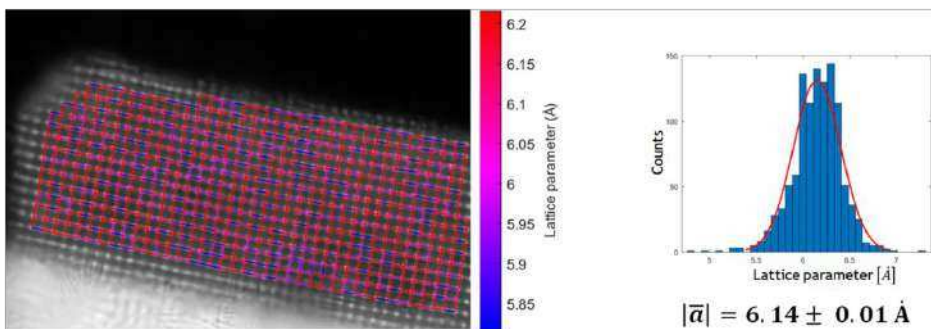
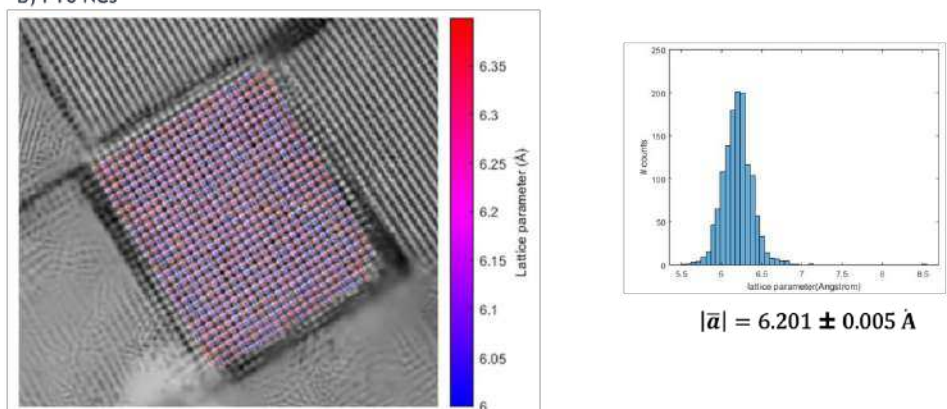


Figure S1. XRD pattern of PT0 (precipitate and supernatant), demonstrating the decreased presence of the KBr phase in the extracted supernatant.

a) Pristine NCs



b) PT0 NCs



c) PT1 NCs

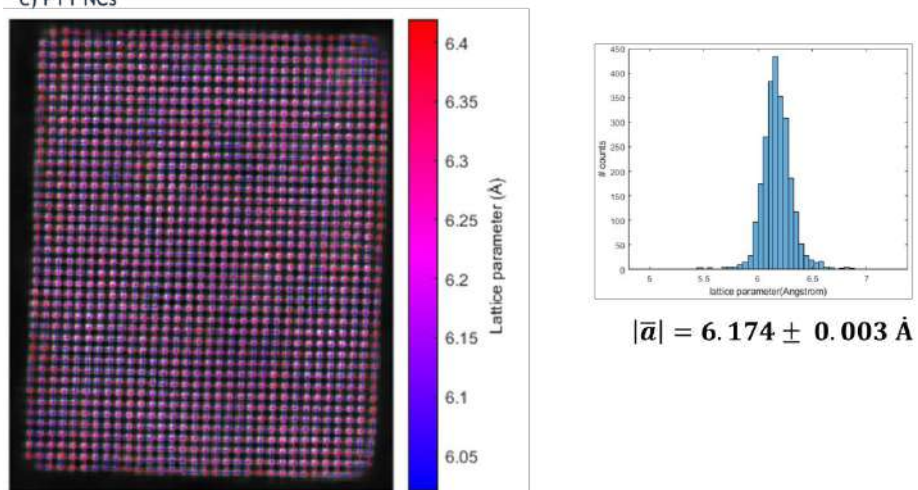


Figure S2. Lattice parameter of a) Pristine, b) PT0, and c) PT1 NCs calculated using StatSTEM.^{1,2} The raw STEM images were restored using a convolutional neural network.²

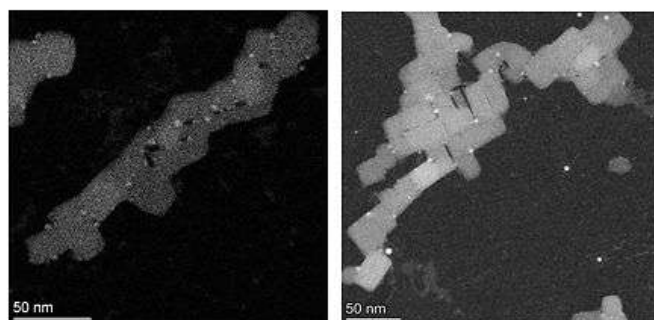


Figure S3. STEM image of PT0, depicting the aggregation of NCs as a result of high surface energy of the NCs (left and right).

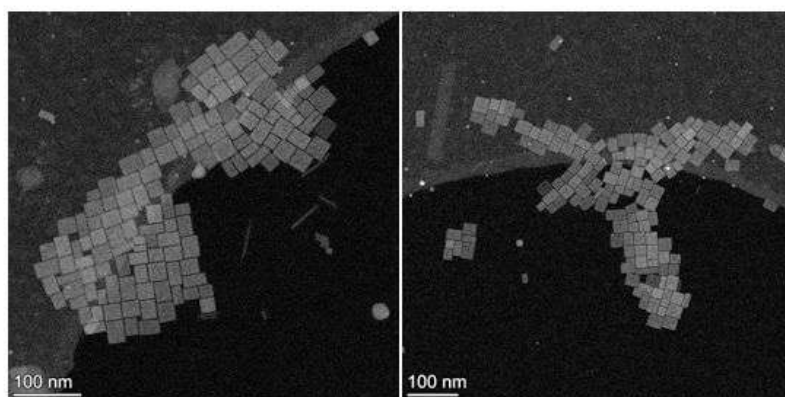


Figure S4. STEM image of PT1 NCs (left and right), depicting a well-defined morphology upon post-treatment.

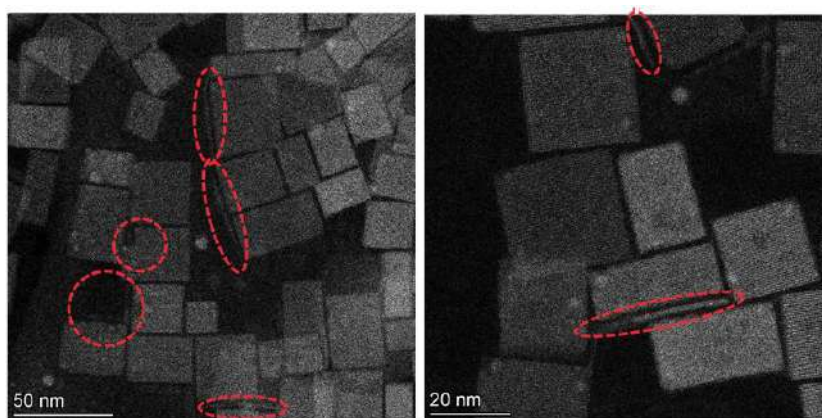


Figure S5. STEM image depicting the vertically aligned PT1 NCs, and indicating the presence of a low-dimensional structures (left and right).

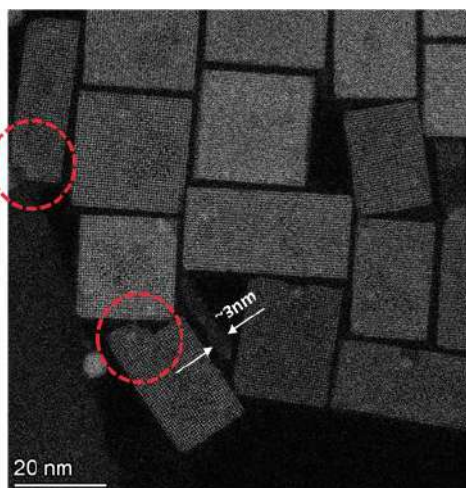


Figure S6. STEM image of PT1 NCs, exhibiting the width of vertically aligned NCs ~ 3 nm as well as the etching of NCs when exposed to ambient conditions (marked with red circles).

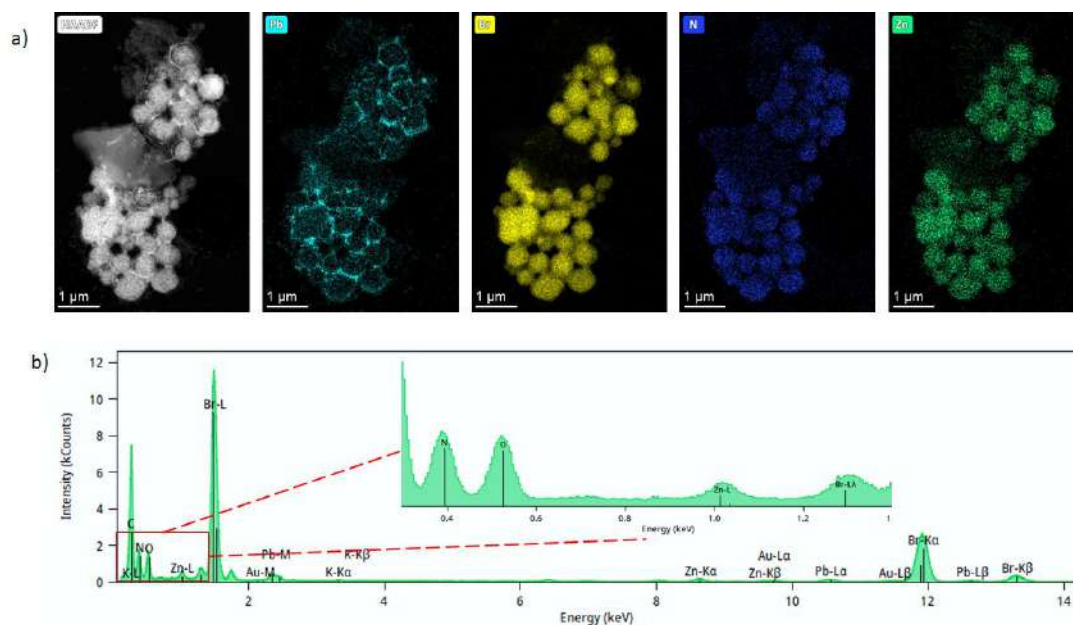


Figure S7. a) EDX elemental mapping of PT1 NCs, exhibiting a region with spherical morphology. The spheres mainly consisted of N and Br, outlined with Pb due to the presence of FAPbBr₃ NCs (at the periphery). b) The EDX spectrum of the area depicted in panel a shows the presence of Zn.

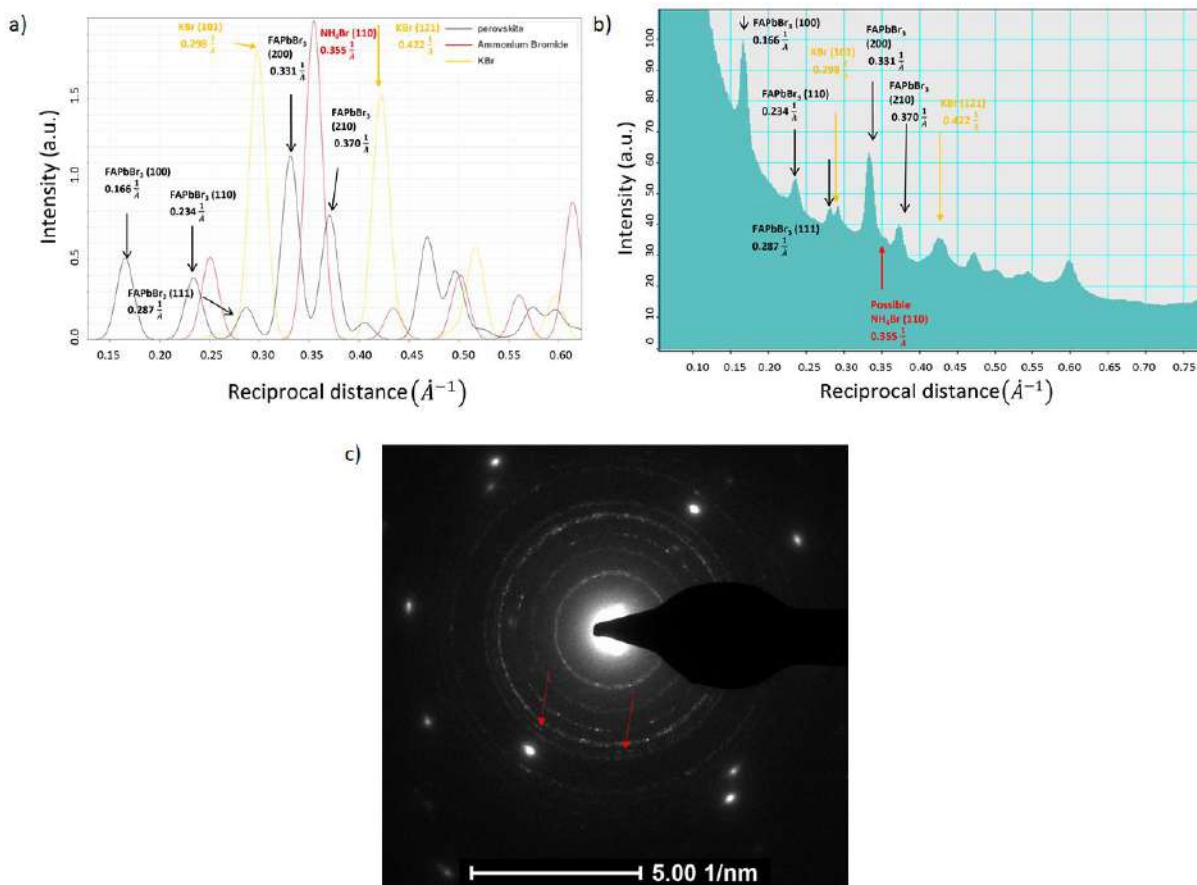


Figure S8. a) Simulated radial diffraction profile from CrystalDiffract indicating the three phases FAPbBr₃, KBr and NH₄Br b) Rotational average from the experimental diffraction pattern shown in c). The arrows indicate the peak position of the three phases FAPbBr₃ (black), KBr (yellow) and NH₄Br (red) c) Experimental diffraction pattern, the NH₄Br diffraction ring is indicated with the red arrows at a reciprocal distance of 0.355 \AA^{-1} .

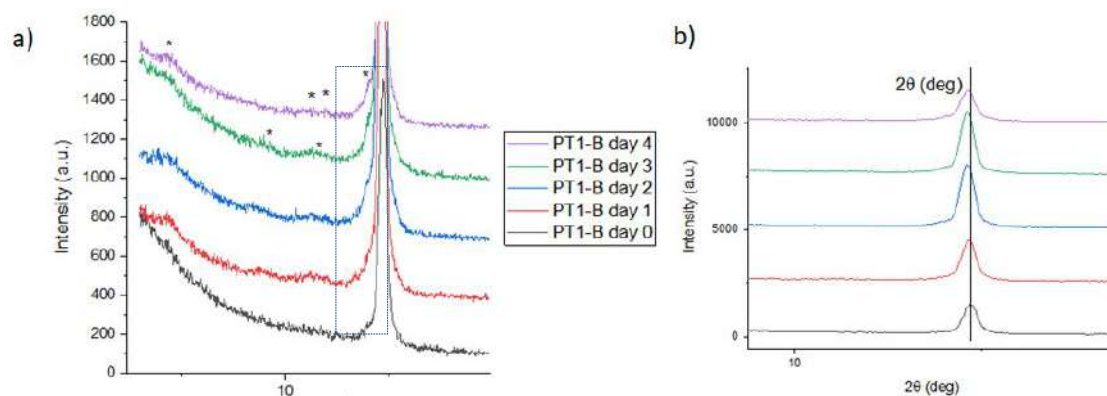


Figure S9. a) XRD pattern of PT1 recorded from day 1 to 5 to test the stability under ambient conditions. The pattern depicts the transition from high to low symmetry upon moisture exposure, indicated by splitting of peaks (marked with dashed box). Furthermore, it also reveals the evolution of 2D phases over time (marked with *) and b) lattice expansion, shifting peaks to lower 2θ, upon exposure to humidity.

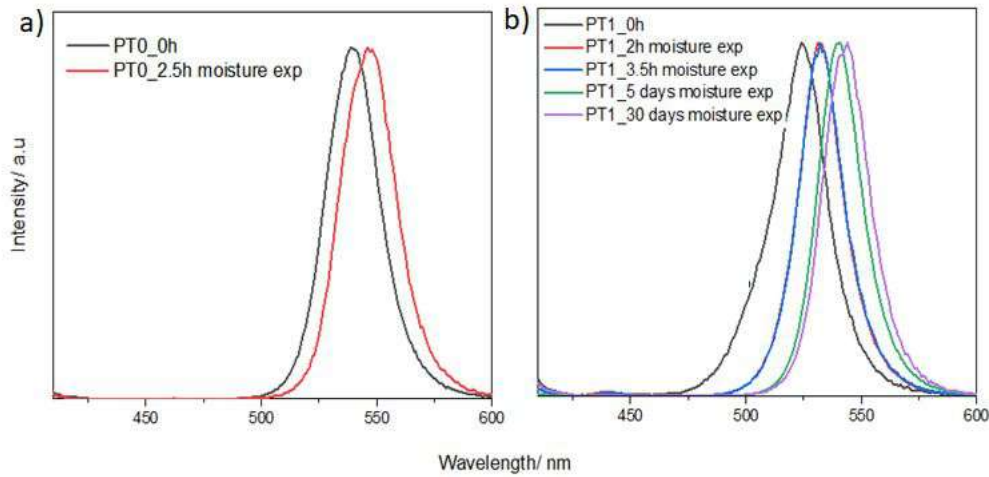


Figure S10. PL spectra of a) PT0, and b) PT1 thin films kept in a chamber with humidity control, relative humidity amounting to 37%. Notably, PT0 was substantially degraded within a few hours of moisture exposure, however, PT1 remained emissive and stable for more than 30 days.

Table S1. Summary of optoelectronic properties and moisture stability of several perovskite structures as reported in the literature.

Perovskites		PL peak maximum (nm)	PLQY (%)	PLQY retained (%)	EQE (%)	Turn-on V	Ref.
CsPbBr ₃ /Cs ₄ PbBr ₆	NCs-Hyflon-DFTHS/OLA ¹	520	73	68 (1 month)	-	-	3
CsPbBr ₃ -polystyrene		525	68	20 – 30 (1 month)	-	-	4
CsPbBr ₃ /CsPb ₂ Br ₅ NCs		520	80	45 (5 days)	-	-	5
CsPbBr ₃ nanosheet		520	82	87 (1 week)	-	-	6
CsPbBr ₃ -PVP-NIPAM polymer ²		515	81	74 (60 min)	-	-	7
NH ₄ PF ₆ -treated CsPbBr ₃		526	83	80 (1 month)	-	-	8
Cs ₃ Cu ₂ I ₅		441	~100	76 (2 month)	-	6	9
CsPbBr ₃ /ZnS		525	-	54 (2 days)	-	-	10
MAPbBr ₃ :SiO ₂		529	88	80 (2 weeks)	-	-	11
FAPbBr ₃		531	95	85 (2 months)	-	-	12
Polystyrene-grafted CsPbBr ₃ NCs		520	94	90 (2 months)	13	-	13
Lead-laurate-treated MAPbBr ₃		528	96	90 (2 months)	-	-	14
FAPbBr ₃ shelled with CsPbBr ₃		504	93	80 (70 days)	8.1	2.6	15
FAPbBr ₃ shelled with Cs ₄ PbBr ₆		525	97	64 (1 month)	-	-	16
FAPbBr ₃		528	83	48 (10 days)	-	2.6	17
KSCN-doped FAPbBr ₃ , post-treated with FABr and ZnBr ₂		520	98	70 (1 month)	1.5	2.4	This work

¹DFTHS/OLA: dodecafluoroheptylpropyl-trihydroxysilane/Oleylamine; ²PVP-NIPAM: polyvinylpyrrolidone and n-isopropyl acrylamide.

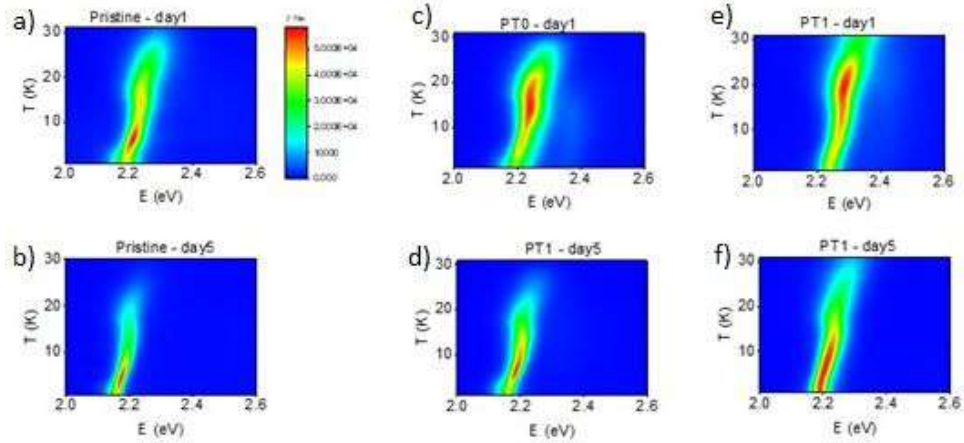


Figure S11. Pseudo-color contour PL mapping at different temperatures on day 1 (top row), and day 5 (bottom row) for a) - b) pristine, c) - d) PT0, and e) - f) PT1 NCs.

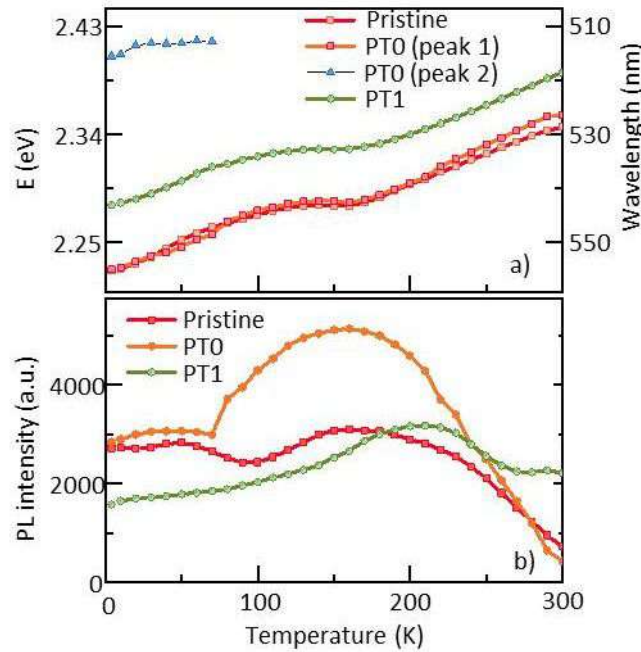


Figure S12. a) PL peak position and b) integrated intensity as a function of temperature for the pristine, PT0, and PT1 on day 1.

The PL spectra at each temperature (4.2 to 300 K at an increment of 10 K) on day 1 for all samples were fitted with the Gauss function and the information related to their peak position and PL integrated intensity were extracted (Figure S11a and b). As can be seen in Figure S12a, for PT0, an extra peak at lower temperatures was observed that has higher energy. This is related to the 2D phase with $n > 4$, as discussed above, which is not visible at room temperature due to the thermal scattering of the charge carriers. This peak is not visible for PT1 and the PL peak also shifts towards higher energy, which is a result of a conglomerate-like structure, as discussed in the TEM study, reminding of a core-shell system.

Table S2. Lifetime parameters obtained for pristine, PT0, and PT1 NCs, recorded on day 1 and day 5.

sample	τ_1 / ns	A_1 (%)	τ_2 / ns	A_2 (%)	τ_3 / μ s	A_3 (%)	$\langle \tau_{avg} \rangle$ / ns
Day 1							
Pristine	10	53	78	38	0.42	9	71
PT0	19	2	296	83	1.47	15	461
PT1	19	7	184	91	1.30	2	200
Day 5							
Pristine	11	56	66	40	0.34	5	55
PT0	12	2	777	93	5.37	6	1000
PT1	19	7	210	93			197

Methods

1. Experimental Procedure

For the synthesis of KSCN:FAPbBr₃ NCs (PT0), a precursor solution consisting of 1 mmol of PbBr₂, 1 mmol of FAPbBr₃ and 0.2 mmol of KSCN dissolved in 2.5 mL of DMF was prepared. From this, 0.25 mL of the precursor solution was injected slowly into a vigorously stirring toluene solution, containing sec-butylamine (s-BA) and oleic acid (OAc) as capping ligands. To ensure colloidal stability, the molar amounts of OAc and s-BA were fixed to 0.5 and 1.1 mmol, respectively. After injection, weakly emissive blue-green luminescent NCs were rapidly formed, and to further promote the precipitation, an extra volume of toluene was subsequently added to the suspension. The resulting NCs were centrifuged at 8000 rpm for 4 min and washed with toluene to remove the excess capping agents and unreacted precursor. The obtained NCs were redispersed in hexane. Since the obtained NCs were weakly emissive, the synthesis procedure was extended by leaving the NC suspension untouched in a vial overnight. This resulted in a color transition from weak blue-green to highly emissive bright green, both in the supernatant and precipitate. Finally, the supernatant was extracted for further studies.

Next, for the post-treatment step, 3 molar equivalents of FAPbBr₃ and 2 molar equivalents of ZnBr₂, equivalent to 0.06 and 0.04 mmol, respectively, were dissolved in hexane, containing OAc and oleylamine (OAm). The resulting mixture was sonicated at 60 °C for 3–4 h, which formed suspension rather than a clear solution. Later, the PT0 NCs were shortly sonicated in this mixture and further centrifuged at 8000 rpm for 4 min. The resulting NCs were redispersed in hexane, yielding bright green emission when exposed to UV lamp.

2. Instrumental Analysis

2.1. X-ray Diffraction

A Malvern PANalytical Empyrean diffractometer using a Debye–Scherrer transmission geometry equipped with a PIXcel3D solid-state detector using a Cu anode. Data were collected on the NC thin films in the range of 1–45° with a step size of 0.0131° and 79 s as counting time.

2.2. Fourier-Transform Infrared Spectroscopy

Attenuated total reflection–FTIR (ATR–FTIR) spectra were recorded on a Varian 670 FTIR spectrometer equipped with a VeeMAXTM III accessory (PikeTech).

2.3. Scanning Transmission Electron Microscopy

High-resolution HAADF-STEM images and Energy Dispersive X-ray Spectroscopy (EDS) was acquired with a probe-corrected cubed Thermo Fisher Scientific Themis Z Microscope, which is equipped with a Super-X EDS detector, operating at 300 kV with a probe semi-convergence angle of 20.5 mrad. Electron diffraction patterns were acquired using a Thermo Fisher Tecnai G2 operating at 200 kV at a camera length of 0.680 m. The lattice parameter of individual NCs was analyzed by using the StatSTEM software.¹ The raw STEM images were restored using a convolutional neural network.²

2.4. UV–Vis Diffuse Reflectance Spectroscopy

Diffuse reflectance spectra (DRS) were recorded on a PerkinElmer Lambda 950 UV–vis–NIR spectrophotometer with the 150 mm integrating sphere accessory in the wavelength range between 400 and 600 nm. The diffuse reflectance (R) data were converted to F(R) using the Kubelka–Munk function: $F(R) = (1 - R)^2 / (2R)$.

2.5. Emission and Excitation Spectroscopy

Excitation and emission spectra were recorded on an Edinburgh Instruments FLS 980 spectrofluorimeter. Samples were measured in front-face mode as thin films created by dropcasting a suspension onto a glass slide that fitted into the Edinburgh solids accessory.

2.6. PL Quantum Yield

Quantum yield measurements were performed on a Horiba Fluorolog 3.22 spectrofluorimeter with an F-3029 integrating sphere accessory fitted with a sample holder to accommodate thin film samples drop casted on a glass slide.

2.7. PL Lifetime Spectroscopy

Nanosecond to millisecond time-resolved luminescence: a 410 nm laser pulse (8 ns, 10 Hz) generated by a system consisting of a pulsed Nd/YAG laser (Quanta-Ray INDI-40, Spectra Physics) was used to excite the samples. The excitation light was focused on the sample by a 150 mm focal length lens, and a small part of this light was sent to a fast photodiode to generate a trigger signal. Right angle configuration between excitation and light collection paths was used, and the luminescence was collected, filtered, and focused on the entrance slit of a 30 cm focal length monochromator. A homemade Labview-based software was used to control and trigger the instruments, read, average, and store the transient data.

2.8. Low-Temperature PL Measurement

For low-temperature PL measurements, the sample was drop-casted on a quartz plate and mounted on an insert in a He flow cryostat, in which the temperature can be varied from 4.2 to 300 K. We used a solid-state laser Thorlabs M365LP1 with driver DC2200 operating at 365 nm for excitation. The laser was coupled to a 550 μm core optical fiber. The PL spectra were collected through 11 core optical fibers of 200 μm diameter that are surrounding the excitation fiber. The detection fibers are coupled to a LOT-QD Shamrock F/4 spectrometer with an electron multiplying charge-coupled detector (EMCCD) iXon DV887. The PL spectra were collected at 5 K increment.

2.9. Device Fabrication and Characterization

The glass/ITO substrates were washed in an ultrasonic bath with soap water, deionized water, acetone, and isopropanol for 10 min, respectively. After drying with nitrogen, they were treated with UV-ozone for 15 min. Then, PEDOT/PSS dispersion (Clevios P VP AI 4083) was spin-coated on the pre-cleaned ITO substrates at 5000 rpm for 60 s, followed by thermal annealing at 110 $^{\circ}\text{C}$ for 20 min. After that, the films were transferred in a N₂-filled glove box, PVK (6mg/ml) in chlorobenzol was spin coated on the substrates at 4000 rpm for 60 s, followed by thermal annealing at 150 $^{\circ}\text{C}$ for 30 min. Finally, 20 mg/mL hexane nanocrystal solution was spin coated on the substrate at 1000 rpm. The devices were finished by evaporation of 40 nm PO-T2T, 1.2 nm LiF, and 120 nm Al layers on top of the perovskite films sequentially. The device area was 0.125 cm², with dimensions of 2.5 mm \times 5 mm. A Thorlabs integrating sphere (IS236A-4), coupled with a calibrated silicon photodiode (SM05PD1B), and a flame spectrometer from Ocean Optics were used to measure the EL intensity and the emission spectrum. The response of the photodiode was calibrated together with the integrating sphere by Thorlabs. The J–V characteristics were measured by an Agilent 4156C Semiconductor Parameter Analyzer, which also records the corresponding light-induced photodiode current at the same time.

References:

- (1) De Backer, A.; van den Bos, K. H. W.; Van den Broek, W.; Sijbers, J.; Van Aert, S. StatSTEM: An Efficient Approach for Accurate and Precise Model-Based Quantification of Atomic Resolution Electron Microscopy Images. *Ultramicroscopy* **2016**, *171*, 104–116.
- (2) Lobato, I.; Friedrich, T.; Van Aert, S. Deep Convolutional Neural Networks to Restore Single-Shot Electron Microscopy Images. arXiv March 29, 2023.
- (3) Lu, Z.; Li, Y.; Xue, Y.; Zhou, W.; Bayer, S.; Williams, I. D.; Rogach, A. L.; Nagl, S. Water-Stable CsPbBr₃/Cs₄PbBr₆ Nanocrystals with a Mixed Fluoropolymer Shell for Optical Temperature Sensing. *ACS Appl. Nano Mater.* **2022**, *5* (4), 5025–5034.
- (4) Wei, Y.; Deng, X.; Xie, Z.; Cai, X.; Liang, S.; Ma, P.; Hou, Z.; Cheng, Z.; Lin, J. Enhancing the Stability of Perovskite Quantum Dots by Encapsulation in Crosslinked Polystyrene Beads via a Swelling–Shrinking Strategy toward Superior Water Resistance. *Advanced Functional Materials* **2017**, *27* (39), 1703535.
- (5) Lou, S.; Zhou, Z.; Xuan, T.; Li, H.; Jiao, J.; Zhang, H.; Gautier, R.; Wang, J. Chemical Transformation of Lead Halide Perovskite into Insoluble, Less Cytotoxic, and Brightly Luminescent CsPbBr₃/CsPb₂Br₅ Composite Nanocrystals for Cell Imaging. *ACS Appl. Mater. Interfaces* **2019**, *11* (27), 24241–24246.
- (6) Xie, M.; Liu, H.; Chun, F.; Deng, W.; Luo, C.; Zhu, Z.; Yang, M.; Li, Y.; Li, W.; Yan, W.; Yang, W. Aqueous Phase Exfoliating Quasi-2D CsPbBr₃ Nanosheets with Ultrahigh Intrinsic Water Stability. *Small* **2019**, *15* (34), 1901994.
- (7) Raj Kar, M.; Patel, U.; Bhaumik, S. Highly Stable and Water Dispersible Polymer-Coated CsPbBr₃ Nanocrystals for Cu-Ion Detection in Water. *Materials Advances* **2022**, *3* (23), 8629–8638.
- (8) Xie, K.; Zhang, S.; Wang, X.; Gong, C.; Zheng, C.; Xiao, W.; Li, F. Post-Synthetic Ammonium Hexafluorophosphate Treatment Enables CsPbBr₃ Perovskite Quantum Dots Exhibiting Robust Photoluminescence and Environmental Stability for White Light-Emitting Diodes. *Journal of Luminescence* **2022**, *252*, 119401.
- (9) Liu, S.; Liu, H.; Zhou, G.; Li, X.; Wang, S. Water-Induced Crystal Phase Transformation of Stable Lead-Free Cu-Based Perovskite Nanocrystals Prepared by One-Pot Method. *Chemical Engineering Journal* **2022**, *427*, 131430.
- (10) Ravi, V. K.; Saikia, S.; Yadav, S.; Nawale, V. V.; Nag, A. CsPbBr₃/ZnS Core/Shell Type Nanocrystals for Enhancing Luminescence Lifetime and Water Stability. *ACS Energy Lett.* **2020**, *5* (6), 1794–1796.
- (11) He, Y.; Yoon, Y. J.; Harn, Y. W.; Biesold-McGee, G. V.; Liang, S.; Lin, C. H.; Tsukruk, V. V.; Thadhani, N.; Kang, Z.; Lin, Z. Unconventional Route to Dual-Shelled Organolead Halide Perovskite Nanocrystals with Controlled Dimensions, Surface Chemistry, and Stabilities. *Science Advances* **2019**, *5* (11), eaax4424.
- (12) Paul, S.; Samanta, A. N-Bromosuccinimide as Bromide Precursor for Direct Synthesis of Stable and Highly Luminescent Green-Emitting Perovskite Nanocrystals. *ACS Energy Lett.* **2020**, *5* (1), 64–69.
- (13) Cai, Y.; Li, W.; Tian, D.; Shi, S.; Chen, X.; Gao, P.; Xie, R.-J. Organic Sulfonium-Stabilized High-Efficiency Cesium or Methylammonium Lead Bromide Perovskite Nanocrystals. *Angewandte Chemie* **2022**, *134* (37), e202209880.

- (14) Chatterjee, S.; Khan, T.; Sen, A.; Das, N.; Sen, P. Massive Amplification of Photoluminescence and Exceptional Water Stability of MAPbBr₃ Nanocrystals through Core–Shell Nanostructure Formation in a Self-Defence Mechanism. *Materials Advances* **2022**, *3* (19), 7360–7369.
- (15) Zhang, C.; Wang, S.; Li, X.; Yuan, M.; Turyanska, L.; Yang, X. Core/Shell Perovskite Nanocrystals: Synthesis of Highly Efficient and Environmentally Stable FAPbBr₃/CsPbBr₃ for LED Applications. *Advanced Functional Materials* **2020**, *30* (31), 1910582.
- (16) Zeng, Y.; Chen, W.; Deng, Y.; Gu, W.; Wu, C.; Guo, Y.; Huang, P.; Liu, F.; Li, H. FAPbBr₃/Cs₄PbBr₆ Core/Shell Perovskite Nanocrystals with Enhanced Stability and Emission: Implications for LEDs. *ACS Appl. Nano Mater.* **2022**, *5* (7), 9534–9543.
- (17) Zu, Y.; Xi, J.; Li, L.; Dai, J.; Wang, S.; Yun, F.; Jiao, B.; Dong, H.; Hou, X.; Wu, Z. High-Brightness and Color-Tunable FAPbBr₃ Perovskite Nanocrystals 2.0 Enable Ultrapure Green Luminescence for Achieving Recommendation 2020 Displays. *ACS Appl. Mater. Interfaces* **2020**, *12* (2), 2835–2841.